Nano Research

Open Access

Research Article

Enhanced polarization switching and superior endurance in $(Hf_{0.5}Zr_{0.5}O_2\text{-}ZrO_2)_n$ nanolaminates via interface engineering

Haiyan Chen[1] ✉, Yang Yang[1], Yuan Yuan[2], Haoran Xie[1], Hang Luo[2], Chuanchang Li[1], and Dou Zhang[2] ✉

[1] *Key Laboratory of Renewable Energy Electric-Technology of Hunan Province, School of Energy and Power Engineering, Changsha University of Science and Technology, Changsha 410114, China*
[2] *State Key Laboratory of Powder Metallurgy, Central South University, Changsha 410083, China*

Cite this article: *Nano Research*, **2026**, *19*, 94908828. https://doi.org/10.26599/NR.2026.94908828

ABSTRACT: Hafnia-based ferroelectric/antiferroelectric (FE/AFE) nanolaminates offer exceptional scalability and complementary-metal-oxide-semiconductor compatibility, making them promising candidates for high-density and low-power memories. However, the deliberate design of periodic interfaces to tailor their ferroelectric performance remains underexplored. Herein, $(Hf_{0.5}Zr_{0.5}O_2\text{-}ZrO_2)_n$ ($(HZO\text{-}ZrO_2)_n$) nanolaminates with different interface numbers (n = 1, 2, 4, 6) are systematically investigated to unveil its impact on polarization, switching dynamics, and device reliability. The $(HZO\text{-}ZrO_2)_2$ configuration achieves an optimal comprehensive performance, exhibiting a large remnant polarization (25.41 μC/cm²), ultrafast switching speed (0.21 μs at 4.8 V), excellent endurance (negligible polarization degradation after 10^8 cycles), and high 10-year retention capability (97.4%). Moreover, the heterogeneous interface between ZrO_2 and $Hf_{0.5}Zr_{0.5}O_2$ can effectively modulate the distribution of oxygen vacancies and polarization-switching barriers. Beyond an optimal number, however, additional interfaces can largely increase the coercive field and hinder domain reversal. These findings provide a powerful design principle for realizing reliable and high-performance hafnia-based ferroelectric memories through interface engineering.

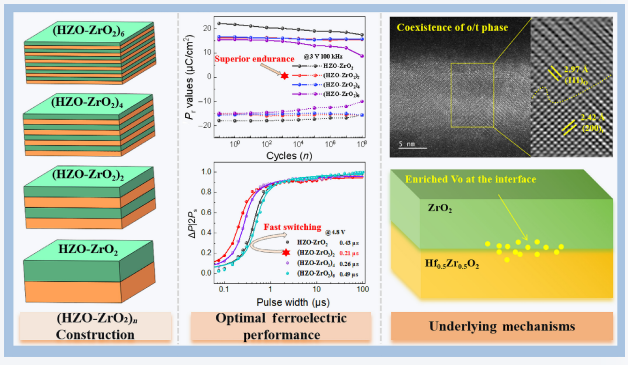

KEYWORDS: $Hf_{0.5}Zr_{0.5}O_2/ZrO_2$, ferroelectric, interface engineering, polarization switching, endurance

1 Introduction

The rapid advancement of the Internet of Things, big data analytics, and artificial intelligence has triggered an exponential growth in global data generation and processing. This surge has created an urgent demand for memory technologies that simultaneously offer high storage density, fast read/write speeds, and low power consumption [1, 2]. Hafnium-based films have attracted great attention for applications in high-performance storage and logic devices primarily due to their robust ferroelectricity at nanometer scales, composition simplicity, and complementary-metal-oxide-semiconductor (CMOS) compatibility [3–5]. As the semiconductor industry continues to push the limits of device miniaturization in the post-Moore era, HfO_2-based ferroelectrics develop into a more scalable and integration alternative compared to those traditional perovskite films [6, 7].

Since the discovery of ferroelectricity in Si-doped HfO_2 [8], numerous studies have been dedicated to investigate the relationship between its internal structure and ferroelectric/antiferroelectric properties, employing diverse strategies including doping elements [9–11], clamping effects [12, 13] and interface engineering [14]. For instance, it has been reported that a smaller crystalline size can effectively reduce the energy barrier for the phase transition from the tetragonal phase to the orthorhombic phase [15–17]. However, the inherent polycrystallinity of these films often results in a random distribution of ferroelectric grains, leading to significant device-to-device performance variability and compromised reliability in memory applications [18]. To overcome these limitations, nanolaminate structures comprising alternating layers of different materials have shown superior ferroelectric performance and grain uniformity compared to solid solutions, thereby offering an efficient pathway towards enhancing the stability of ferroelectric micro-devices [19–21]. Kim et al. has

Received: February 25, 2026; **Revised:** April 21, 2026
Accepted: May 11, 2026

✉Address correspondence to Haiyan Chen, haiyanchen66@csust.edu.cn; Dou Zhang, dzhang@csu.edu.cn

reported that an ultrathin Al_2O_3 interlayer can preserve a stable remnant polarization (P_r) in 40 nm-thick $Hf_{0.5}Zr_{0.5}O_2/Al_2O_3/Hf_{0.5}Zr_{0.5}O_2$ multilayered film [22]. Separately, HfO_2/ZrO_2 superlattices have been successfully developed, exhibiting stable ferroelectricity alongside a low coercive field and excellent stability over a wide thickness range (4–100 nm) [23]. Both the interlayer and superlattice designs can effectively enhance phase transition barriers and inhibit the formation of non-polar phases, resolving the instability of the polar phase and the narrow thickness window in single layered films [24]. The precise regulation between HfO_2 and ZrO_2 films enables further modulation of polarization switching dynamics, driven by the interfacial stress between individual layers [25, 26]. Furthermore, the laminated structure has been shown to reduce leakage current and improve endurance by creating higher energy barriers for oxygen vacancy migration [27, 28]. Overall, nanolaminates deliver superior ferroelectricity and reliability, contributing to synergistic effects including interface coupling, charge blocking, and strain effect between laminates.

Recently, ferroelectric/antiferroelectric (FE/AFE) heterostructures emerged as a powerful strategy, addressing the classic trade-off between high dielectric constant and large P_r values. By precisely tailoring the phase composition of $Hf_{0.5}Zr_{0.5}O_2/ZrO_2$ films, the dielectric constant (ε_r) can be significantly enhanced, an effect that is particularly prominent when the ferroelectric component adopts a mixed-phase boundary composition [29–31]. The FE/AFE bilayer strategy provides a robust guideline for reducing the equivalent oxide thickness in ferroelectric memories [32], as further verified in our previous work [20]. It was also reported that the internal voltage distribution is optimized by creating such a bilayer structure, leading to a significantly reduced coercive field and enhanced polarization [33, 34]. The approach is effective for decreasing the operating voltage in low-power ferroelectric memories and logic devices. While interfaces are universally acknowledged as critical, research has predominantly focused on their presence or on bi-layer configurations. Our previous work has also established an ideal morphotropic phase boundary in an HZO/ZrO_2 bilayer, contributing to both large ε_r and P_r values [19]. Despite these significant advances, the specific role of periodic interfaces in tailoring the intrinsic properties of the film, as well as its consequent effects on polarization behaviors, remains largely unexplored.

In this work, the influence of interface numbers is deeply explored on the ferroelectric polarization, switching rate, and endurance properties of HZO-ZrO_2 FE/AFE thin films. A series of $(HZO\text{-}ZrO_2)_n$ nanolaminates are fabricated and characterized through modulating interface counts (n = 1, 2, 4, 6). The results reveal that a non-monotonic relationship between "n" and overall performance, with the $(HZO\text{-}ZrO_2)_2$ architecture delivering an optimal balance. Concurrently, the resulting sample demonstrated a P_r of 25.41 μC/cm², a coercive field (E_c) of 1.06 MV/cm with the switching time of 0.21 μs at 4.8 V, validating the feasibility of the proposed multiple interfacial numbers in FE/AFE engineering. The presence of interfaces not only promotes the redistribution of oxygen vacancies but also lowers the potential barrier for polarization switching under the stimulation of electric field, thereby optimizing the ferroelectric response and endurance of the film. The present study holds important value for gaining in-depth insights into the performance regulation of hafnium-based ferroelectric thin films, and lays a foundation for their future optimization using interface engineering.

2 Experimental section

2.1 Film deposition and device fabrication

Pt/W/$(HZO\text{-}ZrO_2)_n$/W metal-insulator-metal (MIM) capacitors were fabricated directly on p-typed Si substrates, with the full structural schematic provided in Fig. 1(a). W and Pt electrodes were deposited via direct current (DC) magnetron sputtering under an argon (Ar^+) atmosphere at room temperature (RT). All $(HZO\text{-}ZrO_2)_n$ films were grown by atomic layer deposition (ALD) technique at a chamber temperature of 250 °C. The nanolaminate structures were designed with n = 1, 2, 4, and 6 interfaces by maintaining a constant total thickness of 12 nm while scaling the individual layer thicknesses in a geometric progression. Specifically, the thicknesses of the $Hf_{0.5}Zr_{0.5}O_2$ and ZrO_2 sublayers were set to

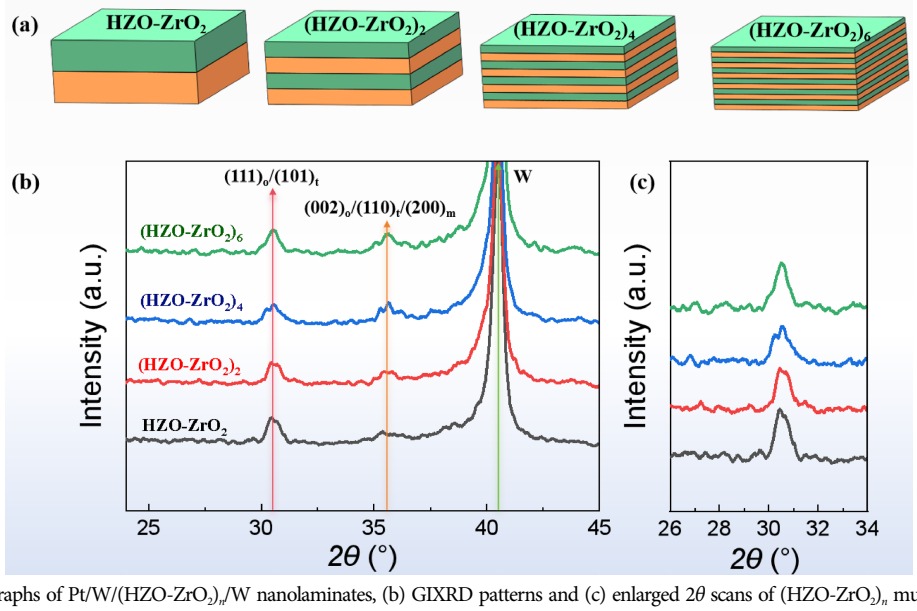

Figure 1 (a) Schematic graphs of Pt/W/$(HZO\text{-}ZrO_2)_n$/W nanolaminates, (b) GIXRD patterns and (c) enlarged 2θ scans of $(HZO\text{-}ZrO_2)_n$ multilayered film from 26° to 34°.

6 nm (n = 1), 3 nm (n = 2), 1.5 nm (n = 4), and 1 nm (n = 6), respectively, to investigate the impact of increasing interface density on the ferroelectric performance. The detailed deposition sequence of Hf and Zr is displayed in Fig. S1 in the Electronic Supplementary Material (ESM). The HZO-ZrO_2 unit corresponds to a FE/AFE bilayer structure ($Hf_{0.5}Zr_{0.5}O_2$-ZrO_2) with a thickness ratio of 1:1. Tetrakis(dimethylamido)hafnium (TDMAH, $Hf[N(CH_3)_2]_4$), tetrakis(dimethylamido)zirconium (TDMAZ, $Zr[N(CH_3)_2]_4$) and deionized H_2O were used as the metalorganic precursors for Hf/Zr and the oxidant for O, respectively. The $Hf_{0.5}Zr_{0.5}O_2$ sublayers were deposited using a 1:1 cycle ratio of HfO_2 and ZrO_2 to ensure stoichiometric balance, with per-cycle growth rates of 0.091 nm for HfO_2 and 0.084 nm for ZrO_2, consistent with our prior work [20]. After deposition, the (HZO-ZrO_2)$_n$ films underwent rapid thermal annealing (RTA) process at 450 °C in an N_2 atmosphere for 60 s. Finally, circular Pt top electrodes (Φ = 200 μm) were patterned on the film surface via DC sputtering at RT using a shadow mask.

2.2 Characterization

Crystallographic structures of all heterogeneous films were identified using a grazing incidence X-ray diffractometer (GIXRD, Smartlab SE) equipped with a Cu Kα radiation source, at a grazing angle of 1°. Elemental species and their chemical bonding states were determined via X-ray photoelectron spectroscopy (XPS, Thermo Fisher Scientific), while all high-resolution XPS spectra were calibrated by normalizing the C 1s peak to 284.8 eV. Polarization–electric field (P–E) loops, current-electric field (I–E) loops, and capacitance–electric field (C–E) curves were analyzed using a ferroelectric testing system (aixACCT TF Analyzer 3000E, Aachen, Germany). Endurance tests for all samples were performed under a voltage of 3 V at a frequency of 100 kHz. First-order reversal curve (FORC) measurements involved saturating the films to positive polarization with a large positive electric field (E_{max}). The electric field was reduced from E_{max} to a reversal field (E_r), and then ramped linearly to E_{max}. The current was recorded during this sweep, and the polarization response yielded a FORC on the P–E curves. The switching density (ρ) was then calculated using Eq. (1)

$$\rho(E_r, E) = \frac{1}{2}\frac{\partial^2 P_{FORC}(E_r, E)}{\partial E_r \partial E} \quad (1)$$

3 Results and discussion

3.1 Crystal structures of (HZO-ZrO_2)$_n$ films

A series of (HZO-ZrO_2)$_n$ heterostructure films were designed according to the schematic architecture as depicted in Fig. 1(a). The sequential increase of interface density is illustrated as the unit number of HZO-ZrO_2 bilayers rises, while the total thickness is maintained at 12 nm. All samples are labeled as HZO-ZrO_2, (HZO-ZrO_2)$_2$, (HZO-ZrO_2)$_4$ and (HZO-ZrO_2)$_6$ to represent 1, 2, 4, and 6 interfaces, respectively. GIXRD measurements were employed to analyze the crystalline phases, as shown in Figs. 1(b) and 1(c). In the wide-angle GIXRD patterns of Fig. 1(b), all samples exhibit a sharp peak around 40°, which is attributed to the W bottom electrode [35] and promises the well crystallization of HfO_2-based films. Additionally, a distinct peak observed at approximately 30.5° corresponding to the $(111)_o/(101)_t$ phases is observed, revealing the coexistence of polar orthorhombic and non-polar tetragonal phases [36]. Notably, the enlarged GIXRD spectra near the main peak show no significant differences among the samples as displayed in Fig. 1(c). Such weak intensity and broad width of the main peak can be ascribed to their small grain size in multilayered films, highlighting the critical role of interface engineering in promoting grain refinement [21]. Furthermore, the presence of $(002)_o/(110)_t/(200)_m$ phases further confirm the coexistence of orthorhombic, tetragonal, and monoclinic phases, indicating that interface engineering induces a complex phase evolution in nanolaminates. However, it is difficult to distinguish these phases due to their quite similar structures.

3.2 Electrical properties of (HZO-ZrO_2)$_n$ films

Electrical characterization of all samples is performed, with results summarized in Fig. 2. P–E hysteresis loops of (HZO-ZrO_2)$_n$ thin films with different numbers of periodic interfaces are presented in Figs. 2(a)–2(d). All measurements were conducted after a wake-up process of 10^3 field cycles at 2 MV/cm, while the initial P–E loops are provided in Fig. S2 in the ESM. Twists in the P–E loops appear with corresponding switching current peaks in the I–E curves (marked by green arrows). These features signify a field-induced phase transition and reflect variations in the distribution of E_c values arising from different periodic interfaces. The HZO-ZrO_2 bilayer film displays well-saturated hysteresis, indicative of robust ferroelectricity. In contrast, the (HZO-ZrO_2)$_2$ film exhibits distorted and less-square hysteresis, which can be attributed to a phase transition from t-phase to o-phase due to the disrupted continuity of ferroelectric $Hf_{0.5}Zr_{0.5}O_2$ by the antiferroelectric ZrO_2 layer. Corresponding I–E loops of these films are displayed in Figs. S3(a)–S3(d) in the ESM. Notably, the current peak intensity weakens as the number of periodic interfaces increases, consistent with the variation in ferroelectric behavior. The appearance of dual current peaks in the (HZO-ZrO_2)$_2$ film indicates that discontinuous t-phase regions can facilitate field-induced phase transitions. In contrast, as the number of interfaces further increases in the (HZO-ZrO_2)$_6$ film, the enhanced interfacial pinning effect significantly increases the energy barrier for polarization switching, leading to the disappearance of these peaks. Figure 2(e) presents the corrected P–E loops acquired via the Positive-Up-Negative-Down (PUND) method, which removes leakage current contributions to ensure accurate polarization measurement. The resulting P_r values are 30.82, 22.21, 19.04, and 18.42 μC/cm^2, respectively, demonstrating a clear decreasing trend.

Figure 2(g) summarizes the P_r and P_m values measured under an applied electric field of 5 V, at which selected to ensure complete saturation across all films. The P_r value decreases from 37.47 to 25.41 μC/cm^2 firstly with interface counts from 1 to 2, and then maintains relatively stable at 21.41 μC/cm^2 for (HZO-ZrO_2)$_4$ and (HZO-ZrO_2)$_6$. This stabilization in nanolaminates with higher interface numbers is ascribed to constrained grain nucleation and growth, along with enhanced surface energy effects [37, 38]. A relatively larger discrepancy between P–E loops and PUND results for the HZO-ZrO_2 bilayer originates from leakage current during domain switching. The dielectric constant versus electric field (ε_r–E) curves for the (HZO-ZrO_2)$_n$ films are shown in Fig. 2(f), which were derived from capacitance–voltage (C–V) measurements at 1 kHz. All films exhibited characteristic butterfly-shaped hysteresis loops, confirming their ferroelectric nature. The ε_r values decrease markedly from 47.5 to 38.84, 29.92, and 27.92 with increasing interface periods (Fig. 2(i)), aligning with the trend in P_r. The coercive field, plotted in Fig. 2(h), first decreases slightly from

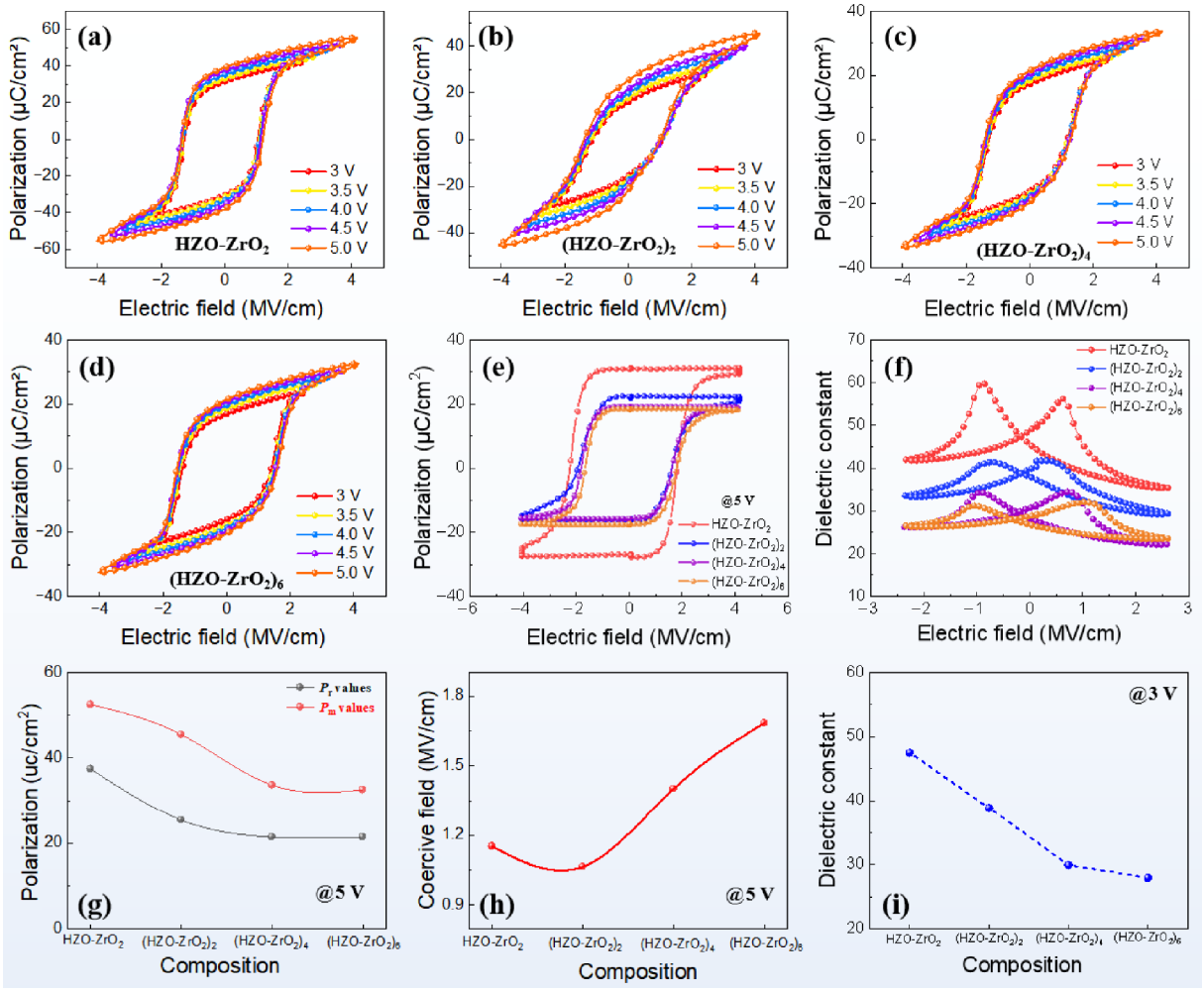

Figure 2 *P*–*E* loops of $(HZO\text{-}ZrO_2)_n$ heterogeneous thin films, (a) $HZO\text{-}ZrO_2$, (b) $(HZO\text{-}ZrO_2)_2$, (c) $(HZO\text{-}ZrO_2)_4$, and (d) $(HZO\text{-}ZrO_2)_6$. (e) Corrected *P*–*E* loops obtained using the PUND method, (f) ε_r–*E* curves, (g) the measured P_m and P_r values at 5 V, (h) comparison of coercive field@5 V, and (i) ε_r values at 3 V for films with different interfaces.

1.15 to 1.06 MV/cm and then rises to 1.68 MV/cm, indicating that domain switching becomes progressively harder with more interfaces. This upward trend stems from the enhanced interfacial pinning effect and inhibited movement of ferroelectric domain wall, requiring a higher electric field to drive polarization switching. Therefore, interface engineering provides an effective pathway to simultaneously achieve high polarization and a low coercive field in HfO_2-based ferroelectric nanolaminates, offering a promising design strategy for high-density, low-power memory applications.

3.3 Endurance performance of $(HZO\text{-}ZrO_2)_n$ films

Reliability remains a critical challenge hindering the practical application of hafnia-based ferroelectrics. To assess the reliability of the $(HZO\text{-}ZrO_2)_n$ nanolaminates, endurance measurements were conducted after the wake-up process. Figure 3(a) displays the uniformity of P_r values for nine devices of each $(HZO\text{-}ZrO_2)_n$ (n = 1, 2, 4, 6) configuration measured at 5 V, showing excellent consistency. This high uniformity is attributed to the precise, layer-by-layer control inherent to ALD, which ensures homogeneous film growth in multilayer structures. It has also been reported that multiple interfaces help maintain fine grains and improve film uniformity [18]. Frequency stability is another key parameter for commercial ferroelectric capacitors. As shown in Fig. S4 in the ESM, the *P*–*E* curves of all devices broaden and shift with increasing frequencies, likely due to built-in electric field and imprint effect [39]. Figure 3(b) reveals that the variation in P_r decreases significantly as the number of periodic interfaces increases. For example, when the frequency increases from 1 to 100 kHz, the P_r drop is reduced from 9.37 μC/cm² for the $HZO\text{-}ZrO_2$ to just 3.07 μC/cm² in the $(HZO\text{-}ZrO_2)_2$ film. The improved frequency stability for more periodic interface can be attributed to the decreased defects in films [40].

Figure 3(c) presents the fatigue performance of all configurations up to 10^8 switching cycles at 3.0 V without any breakdown. The corresponding *P*–*V* loops at selected cycle numbers are shown in Fig. S5 in the ESM, respectively. Notably, the $(HZO\text{-}ZrO_2)_2$ film exhibits superior fatigue resistance, with P_r decreasing slightly from 16.17 to 15.51 μC/cm² after 10^8 cycles. It has also been reported that ZrO_2 layer can effectively suppress charge injection to improve stronger fatigue resistance [41]. In contrast, the $(HZO\text{-}ZrO_2)_6$ film displays noticeable degradation beyond 10^4 cycles, which may be related to its higher E_c value. Prior studies indicate that a lower coercive field helps reduce the operating field and improves the endurance of ferroelectric capacitors [41, 42]. The wake-up effect, a critical yet non-ideal process in practical device operation, was also examined in Fig. S6 in the ESM. The results show that the

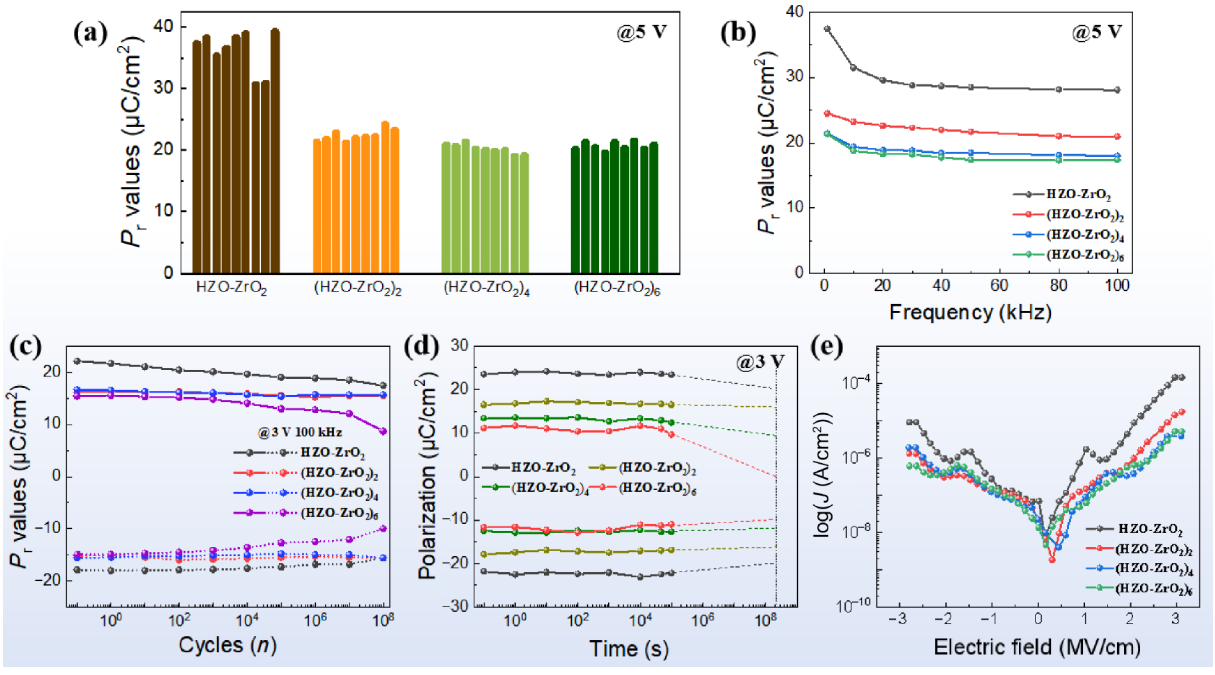

Figure 3 Reliability of Pt/W/(HZO-ZrO_2)$_n$/W MFM capacitors. (a) Uniformity of nine samples, (b) P_r stability under different applied frequencies, (c) fatigue performance with 10^8 cycling numbers at 3 V, (d) retention characteristics, and (e) leakage current density.

polarization evolution during the initial 10^3 cycles becomes less pronounced with increasing individual layer thickness of HZO and ZrO_2. This mitigated wake-up behavior is ascribed to the trapping and detrapping of oxygen vacancies at the electrode-film interface [43, 44]. To provide a comprehensive assessment of all films, retention tests were also performed under the same voltage of 3 V. As shown in Fig. 3(d), the extrapolated 10-year retention rates of P_r for (HZO-ZrO_2)$_n$ films are 87.2%, 97.4%, 70.3%, and 28.3%, respectively with increasing periodic interface from 1 to 6. The (HZO-ZrO_2)$_2$ film demonstrates particularly outstanding data retention. Furthermore, the leakage current characteristics in Fig. 3(e) reveal improved electron-blocking ability with increasing interface number. The periodic multilayer structure can effectively suppress oxygen-vacancy diffusion and homogenization, thereby reducing leakage [45]. Thus, the (HZO-ZrO_2)$_2$ multilayer offers superior reliability, making it a strong candidate for high-endurance memory applications.

3.4 Oxygen vacancy distribution across depth of (HZO-ZrO_2)$_n$ films

XPS was employed to characterize the elemental chemical states and oxygen vacancy concentrations of (HZO-ZrO_2)$_n$ thin films. Prior to XPS measurements, all sample surfaces were cleaned by Ar^+ etching to remove surface contaminants. Figures 4(a)–4(c) display the high-resolution XPS spectra of the O 1s, Zr 3d, and Hf 4f core levels, calibrated using the C 1s reference peak at 284.8 eV. As shown in Fig. 4(a), the O 1s spectrum can be deconvoluted into lattice oxygen and non-lattice oxygen components. The proportion of non-lattice oxygen increases from 8.26% to 12.65% with increasing number of periodic interfaces. To further investigate the location of oxygen vacancies, Zr 3d and Hf 4f peaks were also analyzed. As shown in Figs. 4(b) and 4(c), the intensity of Zr 3d signal increases while the Hf 4f signal attenuates with more periodic interfaces. The observation is primarily attributed to the limited detection depth of XPS and the various concentrations of Hf and Zr within the near-surface region. No significant shifts of binding energy are observed, indicating stable Hf^{4+} and Zr^{4+} bonding environments across the series. Apart from the main peaks, sub-peaks representing lower valence states (ZrO_{2-x} and HfO_{2-x}) are also observed, indicating the existence of non-stoichiometric transition layers. With more periodic interfaces, a notable increase of ZrO_{2-x} contents compared to HfO_{2-x} indicates the aggregation of oxygen vacancies around Zr atoms especially at the HZO/ZrO_2 interfaces.

The above XPS results suggest that the total amount of oxygen vacancies increases, however, these vacancies are likely pinned or dispersed at numerous interlayer interfaces, preventing their long-range migration under an electric field. To verify this point, depth-dependent XPS analysis was performed on the (HZO-ZrO_2)$_2$ thin film with Ar^+ etching at three depths (0, 1, and 2 nm). The evolution of chemical states and elemental distribution with depth is revealed in the O 1s, Zr 3d, and Hf 4f spectra (Fig. S7 in the ESM). The O 1s spectra indicate that the proportion of non-lattice oxygen (O-Zr/O-Hf) decreases from 15.55% at the surface to approximately 10.4% after etching, demonstrating effective removal of surface-adsorbed oxygen species by Ar^+ bombardment. Meanwhile, the ZrO_{2-x} signal shows a marked increase from 9.65% to 13.64% as the etching depth increases from 1 to 2 nm, whereas the HfO_{2-x} concentration rises slightly, confirming the enrichment of vacancies in the ZrO_{2-x} sublayers near the interface. This phenomenon has also been reported in studies using hard X-ray photoemission spectroscopy (HAXPES) for depth-profiling oxygen vacancies [46]. As established by first-principles studies, a controlled concentration of oxygen vacancies can promote the formation of the ferroelectric o-phase [47, 48]. Furthermore, the interfaces act as barriers to oxygen-ion diffusion, kinetically limiting vacancy accumulation and enhancing lattice stability [49, 50]. Therefore, such periodic structure owing oxygen vacancy at heterointerfaces not only stabilize the ferroelectric phase but also prevent the formation of conductive filaments, which can ensure superior fatigue endurance and retention.

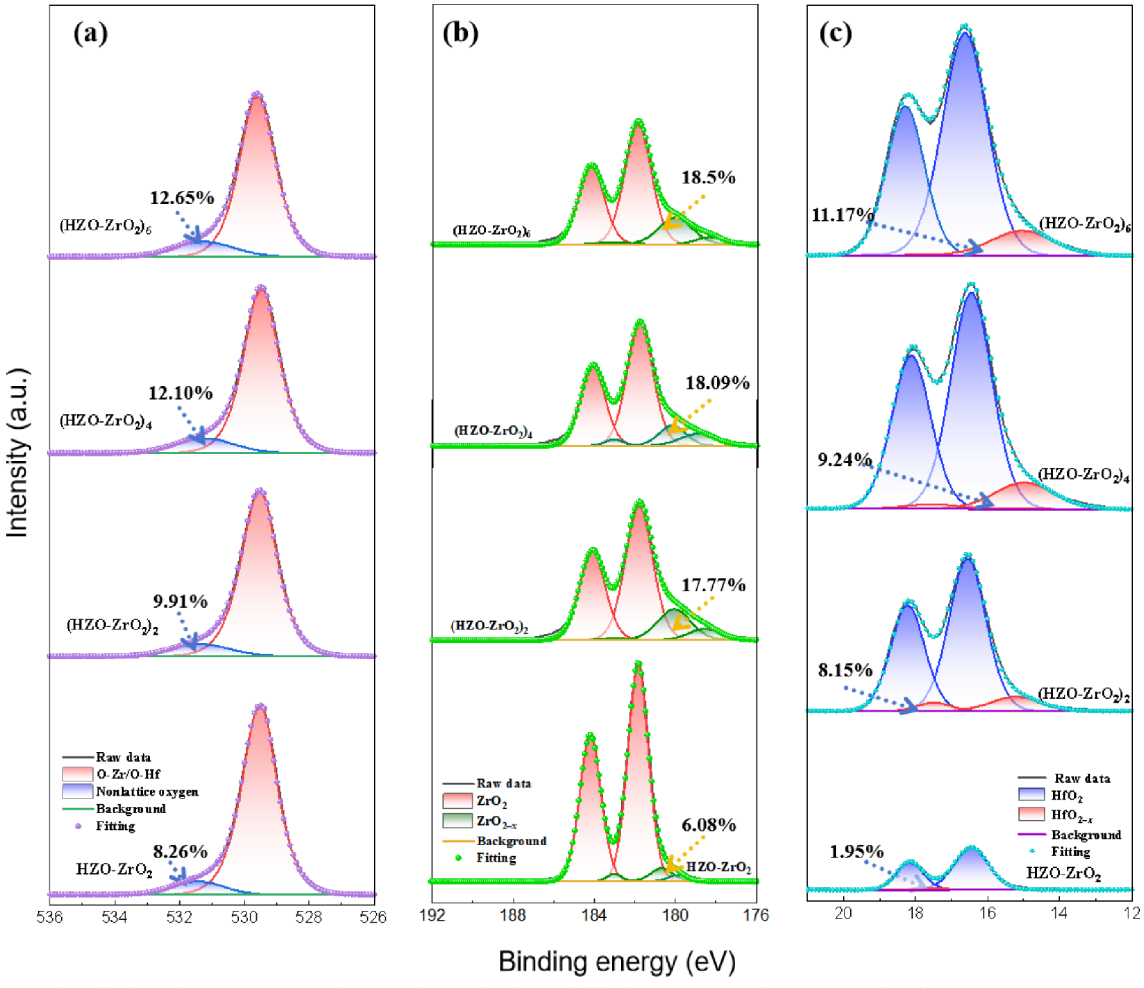

Figure 4 Deconvoluted high-resolution XPS spectra of (a) O 1s, (b) Zr 3d, and (c) Hf 4f for the $(HZO\text{-}ZrO_2)_n$ heterogeneous thin films.

3.5 Analyzation of polarization switching behaviors for $(HZO\text{-}ZrO_2)_n$ films

The FORC method enables a description of domain switching behaviors by resolving the distribution of switching domains and reversible processes [51]. Figures 5(a)–5(d) present the FORC-derived *P*–*E* loops of $(HZO\text{-}ZrO_2)_n$ films with varying cycle numbers (n = 1, 2, 4, 6), where the electric field sweeps are initiated from the positive saturation field region, with corresponding *I*–*E* loops as illustrated in Figs. 5(e)–5(h). Well-defined ferroelectric hysteresis loops are observed for HZO-ZrO_2 and $(HZO\text{-}ZrO_2)_6$ films, whereas the $(HZO\text{-}ZrO_2)_2$ and $(HZO\text{-}ZrO_2)_4$ films exhibit slightly distorted loops. These distinct loop characteristics are also reflected in the corresponding *I*–*E* loops, with the $(HZO\text{-}ZrO_2)_2$ film showing smaller shoulder current peaks. *P*–*E* and *I*–*E* loops confirm robust ferroelectricity, which is also retained even with an increased number of periodic interfaces. Figures 5(i)–5(l) presents the switching density (ρ) distribution as functions of applied electric field (E) and reversal field (E_r). A single and distinct maximum ρ can be observed for all films, indicating concentrated domain switching with uniform field response. The coercive field (E_c) and the internal bias field (E_{bias}) can be extracted from the extreme positions of the FORC density distribution using the relations $E_c = (E - E_r)/2$ and $E_{bias} = (E + E_r)/2$, as summarized in Figs. 5(m)–5(p).

The pronounced peak is located at (E, E_r) position of (1.22, −1.74 MV/cm) for the HZO-ZrO_2 film, with corresponding (E_{bias}, E_c) of (−0.26, 1.51 MV/cm). The compact high-ρ region in the $\rho(E, E_r)$ plot for HZO-ZrO_2 reflects the dominance of reversible domain wall motion. In contrast, for the $(HZO\text{-}ZrO_2)_2$ film, the E_r exhibits a shift toward a more negative value of −1.80 MV/cm, while the E, E_{bias}, and E_c undergo a slight reduction to 1.22, −0.26, and 1.48 MV/cm, respectively. Concurrently, the high-ρ region begins to disperse, which is attributed to the interplay between interfacial stress accumulation and charge trapping. A minor concentrated region near E = 0 also emerges, suggesting the onset of antiferroelectric-like switching. As for the $(HZO\text{-}ZrO_2)_6$ film, (E, E_r) and (E_{bias}, E_c) vary to (1.64, −2.36 MV/cm) and (−0.36, 2.002 MV/cm), respectively. The pronounced negative shift in E_r and the rise in E_c reflect a substantially higher energy barrier for domain reversal, resulting from strong interfacial stress gradients and defect pinning introduced by the numerous HZO/ZrO_2 interfaces. The result confirms that interface engineering can effectively tune the switching barrier in HfO_2-based ferroelectric nanolaminates, providing evidences for the observed macroscopic electrical properties.

To gain deeper insight into the effect of periodic interfaces on the polarization switching dynamics of $(HZO\text{-}ZrO_2)_n$ films, measurements of domain switching kinetics were performed by investigating the nucleation and growth behavior of reverse-polarized ferroelectric domains. Figures 6(a)–6(d) present time-dependent polarization response ($\Delta P/P_s$) for $(HZO\text{-}ZrO_2)_n$ films

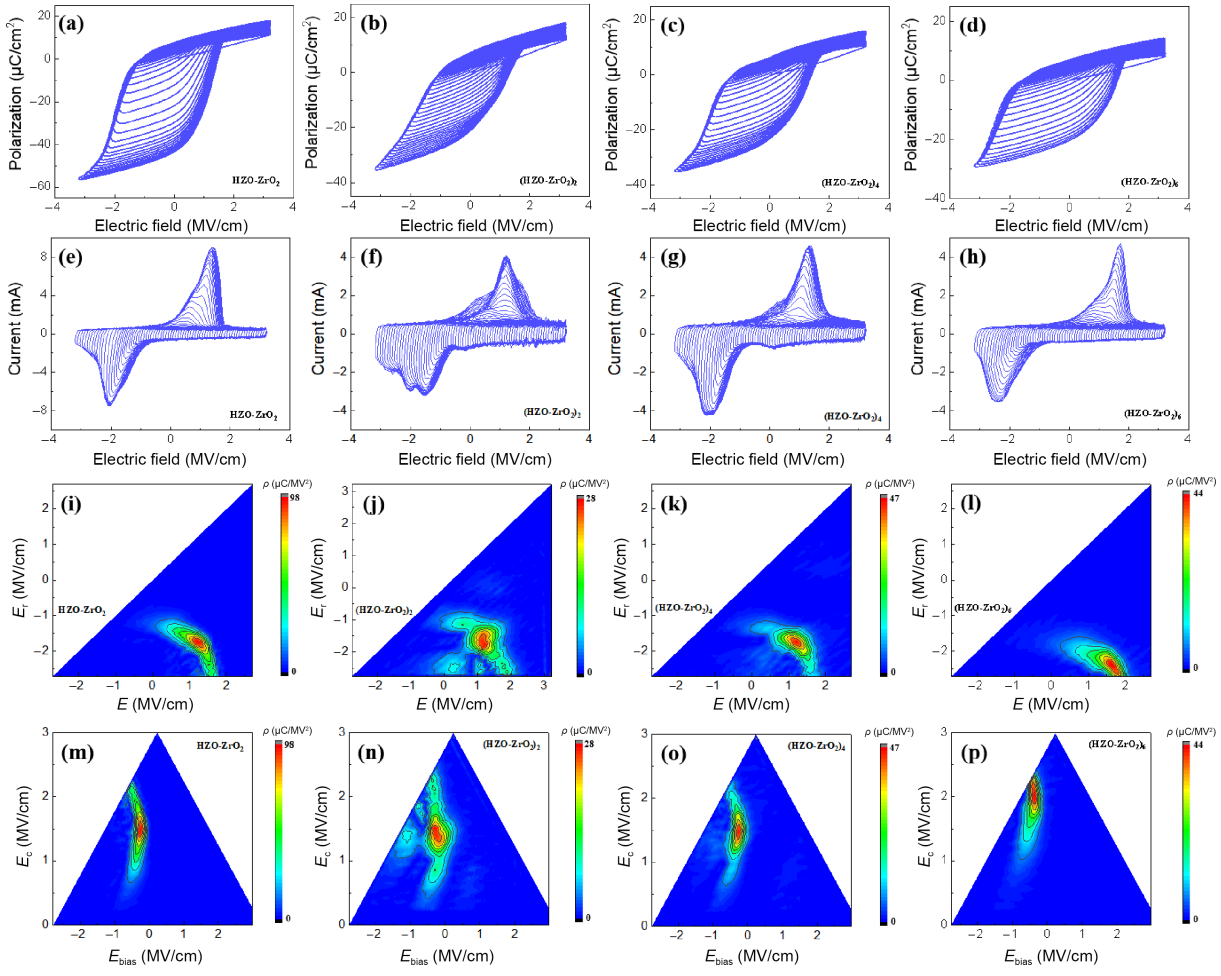

Figure 5 FORC switching density distribution of $(HZO/ZrO_2)_n$ thin films (n = 1, 2, 4, 6). (a)–(d) P–E loops, (e)–(h) I–E loops, (i)–(l) $\rho(E, E_r)$ plots, and (m)–(p) $\rho(E_{bias}, E_C)$ plots.

under voltages ranging from 3.2 to 4.8 V with a voltage step of 0.6 V. The corresponding Lorentzian distribution characteristics of switching times are further extracted from the fitted functions, and the results are displayed in Figs. 6(e)–6(h). The detailed pulse waveform is depicted in Fig. S8 in the ESM, where the rectangular write pulse width (denoted as time (t)) ranges from 50 ns to 100 μs. The polarization response accelerates significantly with increasing voltage regardless of their heterogeneous interfaces. This trend aligns well with the nucleation-limited switching (NLS) model according to the relationship given by Eq. (S1) in the ESM, which have also been reported in previous investigations [52–54]. The detailed fitting results are displayed in Table S1 in the ESM. For the $HZO-ZrO_2$ film, $\Delta P/P_s$ approaches the saturation value of 1 within only ~ 1 μs at 4.8 V, whereas reaching a similar level requires over 4.8 μs at the applied voltage of 3 V. According to NLS model, a higher electric field provides a stronger driving force for ferroelectric domain wall motion, thus accelerating domain switching process.

The $(HZO-ZrO_2)_2$ film exhibits the fastest polarization switching speed among all samples, as indicated by a comparison of polarization response under the same write pulse amplitude of 4.8 V (Fig. S9(a) in the ESM). The trend aligns with its lower E_c values as shown in Fig. 2(f), as a smaller E_c is recognized to enable faster polarization switching [55, 56]. Also, the existence of antiferroelectric t-phase has been reported to effectively lower the energy barrier for polarization reversal, thereby accelerating rapid switching [57]. A trend of initial decrease followed by an increase in t_1 values is observed for the $(HZO-ZrO_2)_n$ films from the Lorentzian distributions at 3 and 4.8 V, as displayed in Fig. S9(b) in the ESM. The polarization switching speed of the $(HZO-ZrO_2)_2$ film can reach 0.21 μs at 4.8 V, highlighting the advantage of the multilayer architecture. The activation energy (E_a) for polarization switching was extracted by fitting the field-dependent switching times according to the Merz equation (Eq. (S3) in the ESM). Figure 6(i) presents the corresponding linear relationship between $\log(t)$ and $1/E$, yielding the E_a values of 3.30 MV/cm for $HZO-ZrO_2$, 3.01 MV/cm for $(HZO-ZrO_2)_2$, 3.40 MV/cm for $(HZO-ZrO_2)_4$, and 6.66 MV/cm for $(HZO-ZrO_2)_6$. The $(HZO-ZrO_2)_2$ film exhibits accelerated polarization switching due to its lower E_c and E_a values, which facilitate reversed-domain nucleation. Notably, a significantly higher E_a in the $(HZO-ZrO_2)_6$ film is attributed to the combined effects of interfacial pinning and grain boundary constraints. More oxygen vacancies and structural defects can be introduced as the sublayer thickness decreases, which act as potent pinning sites and consistent with XPS results. These defects significantly enhance the energy barrier for domain nucleation and hinder domain wall propagation, thereby requiring a much higher electric field to trigger polarization switching. The dramatic increase in E_a is highly consistent with the observed enhancement of the coercive field as shown in Fig. 2(h). It was also verified that heterointerfaces can

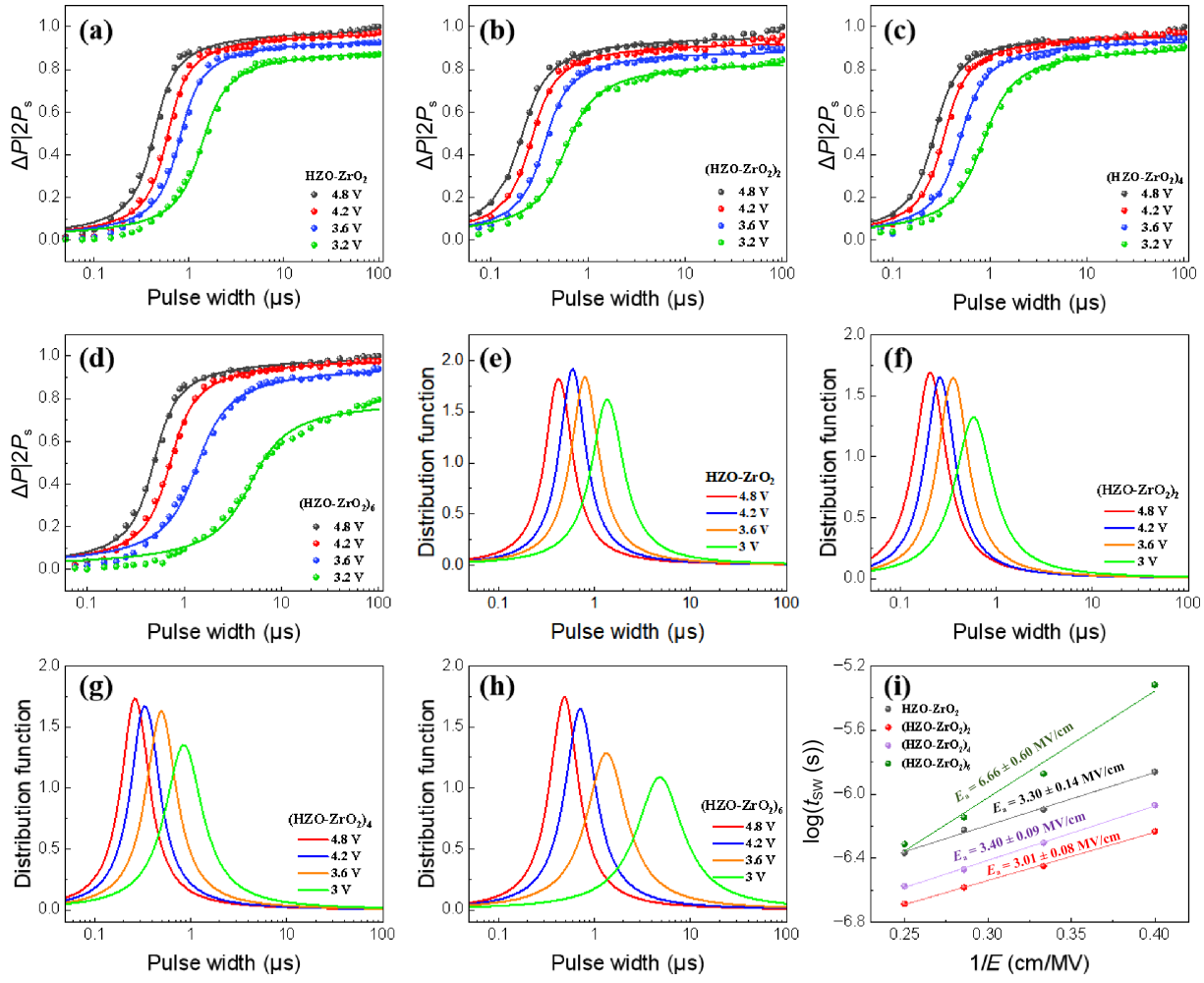

Figure 6 Polarization switching kinetics based on NLS model. Normalized switched polarization ($\Delta P/P_s$) as a function of pulse width for (a) HZO-ZrO_2, (b) (HZO-ZrO_2)$_2$, (c) (HZO-ZrO_2)$_4$, and (d) (HZO-ZrO_2)$_6$ films under different applied voltages. Corresponding Lorentzian distribution functions of switching times fitted with the NLS model for (e) HZO-ZrO_2, (f) (HZO-ZrO_2)$_2$, (g) (HZO-ZrO_2)$_4$ and (h) (HZO-ZrO_2)$_6$ films. (i) Activation field (E_a) derived from the electric-field dependence of the characteristic switching time.

lower the energy barrier for uniform switching and domain-wall motion [58]. This faster switching also implies a shorter charge-injection period, which contributes to the improved fatigue endurance observed in Fig. 3(c). Excessive interfaces in the (HZO-ZrO_2)$_6$ film appear to hinder polarization switching and degrade fatigue performance, demonstrating that engineering the number of interfaces provides an effective method for modulating switching kinetics. To further evaluate the competitive advantages of (HZO-ZrO_2)$_2$ nanolaminates, a comprehensive benchmark comparison with state-of-the-art HZO-based ferroelectric films is summarized in Table S2 in the ESM. Compared to pure HZO films and other multilayer systems [19, 59–67], this work achieves a superior balance of high remnant polarization, ultra-fast switching speed, and excellent fatigue endurance. Notably, the optimized interface engineering not only enhances the switching kinetics but also ensures robust reliability, positioning the nanolaminate as a promising candidate for high-performance non-volatile memory applications.

3.6 Atomic characterization between HZO and ZrO_2 interface

To better understand the structural origin of the antiferroelectric transition, atomic-resolution microstructural characterizations of the (HZO-ZrO_2)$_2$ thin film was conducted using scanning transmission electron microscopy (STEM) and high angle annular dark-field (HAADF) techniques. As revealed by the cross-sectional TEM bright-field image shown in Fig. 7(a), the heterostructure exhibits a highly periodic stacking sequence of HZO and ZrO_2 sublayers. Each oxide functional layer presents uniform thickness of approximately 3 nm, demonstrating excellent controllability of the atomic layer deposition process. Elemental distribution and interfacial interdiffusion were further examined by energy-dispersive X-ray spectroscopy (EDS) mapping, as shown in Fig. 7(b). The sharp compositional contrast between adjacent layers indicates atomically flat interfaces, which is important for achieving excellent electrical isolation and low leakage current. It also reveals that Zr exhibits higher diffusivity than Hf, leading to a chemically graded interface enriched in oxygen vacancies, consistent with the XPS analysis. The localized distribution of oxygen vacancies is believed to help reduce the energy barrier for domain switching, partly explaining the faster polarization switching speed observed in this sample. The corresponding EDS spectrum (Fig. 7(c)) confirms the presence of Hf, Zr, W, and O elements, with characteristic peaks (W–M, Hf–M, Zr–L, Hf–Lα, W–Lα) matching the designed

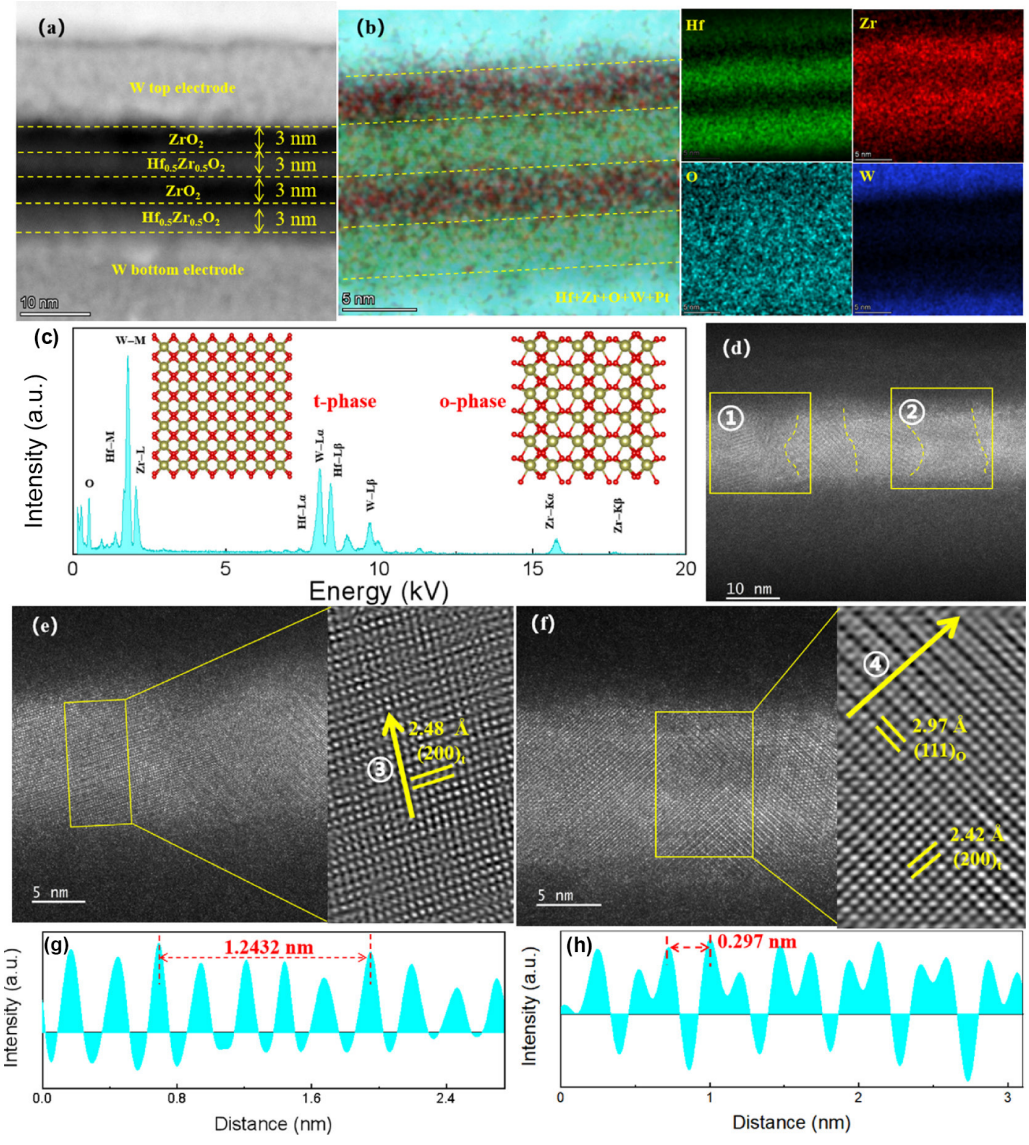

Figure 7 Structural characterizations of MFM capacitors with $(HZO\text{-}ZrO_2)_2$ thin films. (a) High-resolution cross-sectional TEM images, (b) HAADF-STEM image and corresponding EDS mapping of Hf, Zr, W, and O elements, (c) EDS spectra collected from the HAADF-TEM in (b), (d) HRTEM images presenting multiphases, (e) and (f) HRTEM images from area ① and ② in (d) and corresponding enlarged view of the selected highlighted area. (g) and (h) Two line scans of the atomic columns within the dashed rectangles framed in (e) and (f).

composition. The extracted atomic percentages from EDS are 7.57% and 23.47% for Hf and Zr, yielding a Hf:Zr atomic ratio close to 1:3, in agreement with the design schematic in Fig. 1(a).

Figure 7(d) shows a low-magnification TEM overview with typical multiphases, with regions ① and ② selected for high-resolution TEM (HRTEM) analysis. As shown in Fig. 7(e) for region ①, HRTEM imaging reveals well-resolved lattice fringes with an interplanar spacing of 2.48 Å, corresponding to the (200) plane of t-phase. In contrast, region ② (Fig. 7(f)) exhibits lattice fringes with spacings of 2.97 and 2.42 Å, corresponding to the (111) plane of the o-phase and the (200) plane of the t-phase, respectively. Intensity profiles scanned along the (200) and (111) directions in Figs. 7(e) and 7(f) are plotted in Figs. 7(g) and 7(h), confirming the compositional modulation and periodic structural variations of the film at the nanoscale. The coexistence of the t-phase and o-phase can contribute to its lower coercive field and activation energy observed in the above electrical measurements.

4 Conclusions

In conclusion, this work establishes a powerful structural design strategy for the optimization of ferroelectric performance and device reliability by precisely engineering periodic $(HZO\text{-}ZrO_2)_n$ interfaces. The $(HZO\text{-}ZrO_2)_2$ heterostructure exhibits superior characteristics, including a rapid switching speed (0.21 μs at 4.8 V) and a lower coercive field of 1.06 MV/cm (at 5 V). The enhanced performance can be attributed to the coexistence of the antiferroelectric t-phase and ferroelectric o-phase. Furthermore, interfacial oxygen vacancies verified by XPS and TEM analysis facilitate phase transition from t-phase to o-phase, thus resulting in a reduced activation field for domain switching. After initial wake-up process, the device exhibits a robust remnant polarization with negligible degradation after 10^8 cycles, alongside with excellent data retention over 10 years and ultralow leakage current. These results not only offer deeper insights into interface engineering of HfO_2-

based thin films, but also provide a feasible pathway toward low-power, high-reliability electronic devices.

Electronic Supplementary Material: Supplementary material (process flowchart, initial *P*–*E* loops, *I*–*E* loops, *P*–*E* loops at different frequencies and cycles, wake-up curves, XPS spectra, NLS fitting results and performance comparison) is available in the online version of this article at https://doi.org/10.26599/NR.2026.94908828.

Data availability

All data needed to support the conclusions in the paper are presented in the manuscript and the Electronic Supplementary Material. Additional data related to this paper may be requested from the corresponding author upon request.

Acknowledgements

This work is supported by the National Natural Science Foundation of China (No. 52302217), the Natural Science Foundation in Hunan Province of China (No. 2024JJ6028), the Excellent Youth Program of the Hunan Provincial Department of Education (No. 25B0210), and Project supported by State Key Laboratory of Powder Metallurgy, Central South University, Changsha, China (No. Sklpm-KF-2025019).

Declaration of competing interest

All the contributing authors report no conflict of interests in this work.

Author contribution statement

H. Y. C.: Conceptualization, review & editing, funding acquisition. Y. Y. (Yang Yang): Data curation, investigation, writing manuscript. Y. Y. (Yuan Yuan): Validation, investigation. H. R. X.: Methodology, supervision. H. L.: Methodology, supervision. C. C. L.: Supervision, project administration. D. Z.: Project administration, resources. All the authors have approved the final manuscript.

Use of AI statement

None.

References

[1] Khan, A. I.; Keshavarzi, A.; Datta, S. The future of ferroelectric field-effect transistor technology. *Nat. Electron.* **2020**, *3*, 588–597.

[2] Martin, L. W.; Rappe, A. M. Thin-film ferroelectric materials and their applications. *Nat. Rev. Mater.* **2016**, *2*, 16087.

[3] Liao, J. J.; Dai, S. W.; Peng, R. C.; Yang, J. H.; Zeng, B. J.; Liao, M.; Zhou, Y. C. HfO_2-based ferroelectric thin film and memory device applications in the post-Moore era: A review. *Fund. Res.* **2023**, *3*, 332–345.

[4] Wei, Y. F.; Nukala, P.; Salverda, M.; Matzen, S.; Zhao, H. J.; Momand, J.; Everhardt, A. S.; Agnus, G.; Blake, G. R.; Lecoeur, P. et al. A rhombohedral ferroelectric phase in epitaxially strained $Hf_{0.5}Zr_{0.5}O_2$ thin films. *Nat. Mater.* **2018**, *17*, 1095–1100.

[5] Schroeder, U.; Park, M. H.; Mikolajick, T.; Hwang, C. S. The fundamentals and applications of ferroelectric HfO_2. *Nat. Rev. Mater.* **2022**, *7*, 653–669.

[6] Zhou, Z. P.; Li, L. Q.; Feng, Y.; Wang, X. L.; Zheng, Z. J.; Jiao, L. M.; Zheng, H. F.; Shi, Y. F.; Ang, K. W.; Gong, X. Advancing the frontiers of HfO_2-based ferroelectric memories: Innovative concepts from materials to applications. *Adv. Mater.* **2025**, *37*, e09525.

[7] Chen, Y. T.; Yang, Y.; Yuan, P.; Jiang, P. F.; Wang, Y.; Xu, Y. N.; Lv, S. X.; Ding, Y. X.; Dang, Z. W.; Gao, Z. M. et al. Flexible $Hf_{0.5}Zr_{0.5}O_2$ ferroelectric thin films on polyimide with improved ferroelectricity and high flexibility. *Nano Res.* **2022**, *15*, 2913–2918.

[8] Böscke, T. S.; Müller, J.; Bräuhaus, D.; Schröder, U.; Böttger, U. Ferroelectricity in hafnium oxide thin films. *Appl. Phys. Lett.* **2011**, *99*, 102903.

[9] Müller, J.; Böscke, T. S.; Schröder, U.; Mueller, S.; Bräuhaus, D.; Böttger, U.; Frey, L.; Mikolajick, T. Ferroelectricity in simple binary ZrO_2 and HfO_2. *Nano Lett.* **2012**, *12*, 4318–4323.

[10] Schenk, T.; Fancher, C. M.; Park, M. H.; Richter, C.; Künneth, C.; Kersch, A.; Jones, J. L.; Mikolajick, T.; Schroeder, U. On the origin of the large remanent polarization in La: HfO_2. *Adv. Electron. Mater.* **2019**, *5*, 1900303.

[11] Liu, X.; Yao, L. L.; Cheng, Y. H.; Xiao, B.; Liu, M.; Wang, W. K. Observing large ferroelectric polarization in top-electrode-free Al: HfO_2 thin films with Al-rich strip structures. *Appl. Phys. Lett.* **2019**, *115*, 152901.

[12] Kim, S. J.; Narayan, D.; Lee, J. G.; Mohan, J.; Lee, J. S.; Lee, J.; Kim, H. S.; Byun, Y. C.; Lucero, A. T.; Young, C. D. et al. Large ferroelectric polarization of $TiN/Hf_{0.5}Zr_{0.5}O_2/TiN$ capacitors due to stress-induced crystallization at low thermal budget. *Appl. Phys. Lett.* **2017**, *111*, 242901.

[13] Lomenzo, P. D.; Takmeel, Q.; Zhou, C. Z.; Fancher, C. M.; Lambers, E.; Rudawski, N. G.; Jones, J. L.; Moghaddam, S.; Nishida, T. TaN interface properties and electric field cycling effects on ferroelectric Si-doped HfO_2 thin films. *J. Appl. Phys.* **2015**, *117*, 134105.

[14] Cheema, S. S.; Shanker, N.; Wang, L. C.; Hsu, C. H.; Hsu, S. L.; Liao, Y. H.; San Jose, M.; Gomez, J.; Chakraborty, W.; Li, W. S. et al. Ultrathin ferroic HfO_2-ZrO_2 superlattice gate stack for advanced transistors. *Nature* **2022**, *604*, 65–71.

[15] Shandalov, M.; Mcintyre, P. C. Size-dependent polymorphism in HfO_2 nanotubes and nanoscale thin films. *J. Appl. Phys.* **2009**, *106*, 084322.

[16] Pitcher, M. W.; Ushakov, S. V.; Navrotsky, A.; Woodfield, B. F.; Li, G. S.; Boerio-Goates, J.; Tissue, B. M. Energy crossovers in nanocrystalline zirconia. *J. Am. Ceram. Soc.* **2005**, *88*, 160–167.

[17] Tao, L.; Zhang, Y. F.; Du, S. X. The origin of stability and ferroelectricity in non-stoichiometric rhombohedral $Hf(Zr)_{1+x}O_2$. *Sci. China Mater.* **2024**, *67*, 1282–1287.

[18] Liu, Y. S.; Su, P. Variability analysis for ferroelectric FET nonvolatile memories considering random ferroelectric-dielectric phase distribution. *IEEE Electron Dev. Lett.* **2020**, *41*, 369–372.

[19] Liu, L.; Jiang, C. F.; Yuan, X.; Zhang, Y.; Chen, H. Y.; Zhang, D. Large ferroelectric polarization and high dielectric constant in HfO_2-based thin films via $Hf_{0.5}Zr0_5O_2/ZrO_2$ nanobilayer engineering. *J. Materiomics* **2025**, *11*, 100922.

[20] Liu, L.; Jiang, C. F.; Yuan, X.; Zhang, Y.; Chen, H. Y.; Zhang, D. Ultrathin fluorite nanobilayer films with excellent ferroelectricity for high-density memory applications. *J. Mater. Sci. Technol.* **2026**, *241*, 219–228.

[21] Cheema, S. S.; Kwon, D.; Shanker, N.; Dos Reis, R.; Hsu, S. L.; Xiao, J.; Zhang, H. G.; Wagner, R.; Datar, A.; McCarter, M. R. et al. Enhanced ferroelectricity in ultrathin films grown directly on silicon. *Nature* **2020**, *580*, 478–482.

[22] Kim, H. J.; Park, M. H.; Kim, Y. J.; Lee, Y. H.; Jeon, W.; Gwon, T.; Moon, T.; Kim, K. D.; Hwang, C. S. Grain size engineering for ferroelectric $Hf_{0.5}Zr_{0.5}O_2$ films by an insertion of Al_2O_3 interlayer. *Appl. Phys. Lett.* **2014**, *105*, 192903.

[23] Li, J. X.; Deng, S. Q.; Ma, L. Y.; Si, Y. Y.; Zhou, C.; Wang, K. F.; Huang, S. Z.; Yang, J. Y.; Tang, Y. L.; Ku, Y. C. et al. Enhancing ferroelectric stability: Wide-range of adaptive control in epitaxial HfO_2/ZrO_2 superlattices. *Nat. Commun.* **2025**, *16*, 6417.

[24] Wang, Y. F.; Zhu, C. Q.; Sun, H. J.; Wang, W. L.; Zou, L. Q.; Yi, Y. H.; Xu, J. Y.; Ren, J. W.; Hu, S.; Ye, L. et al. Phase transition kinetics and sublayer optimization of HfO_2/ZrO_2 superlattice ferroelectric thin films. *Appl. Phys. Lett.* **2024**, *125*, 083503.

[25] Ke, X. Y.; Chai, J. S.; Shao, X. Z.; Duan, J. H.; Sun, X. Q.; Yang, S.; Xiang, J. J.; Han, K.; Wang, Y. R.; Xu, H. et al. Switching dynamics of HfO_2-ZrO_2 nanolaminates with different laminate thicknesses. *IEEE Trans. Electron Dev.* **2024**, *71*, 3651–3658.

[26] Migita, S.; Ota, H.; Asanuma, S.; Morita, Y.; Toriumi, A. Accelerated ferroelectric phase transformation in HfO_2/ZrO_2 nanolaminates. *Appl. Phys. Express* **2021**, *14*, 051006.

[27] Kumar, M.; Han, S. I.; Ahn, Y.; Jeon, Y.; Park, J.; Seo, H. Switchable polar nanotexture in nanolaminates HfO_2–ZrO_2 for ultrafast logic-in-memory operations. *Small* **2023**, *19*, 2206736.

[28] Liang, Y. K.; Li, W. L.; Wang, Y. J.; Peng, L. C.; Lu, C. C.; Huang, H. Y.; Yeong, S. H.; Lin, Y. M.; Chu, Y. H.; Chang, E. Y. et al. ZrO_2–HfO_2 superlattice ferroelectric capacitors with optimized annealing to achieve extremely high polarization stability. *IEEE Electron Dev. Lett.* **2022**, *43*, 1451–1454.

[29] Kashir, A.; Ghiasabadi Farahani, M.; Kamba, S.; Yadav, M.; Hwang, H. $Hf_{1-x}Zr_xO_2/ZrO_2$ nanolaminate thin films as a high-κ dielectric. *ACS Appl. Electron. Mater.* **2021**, *3*, 5632–5640.

[30] Kashir, A.; Ghiasabadi Farahani, M.; Hwang, H. Towards an ideal high-κ HfO_2–ZrO_2-based dielectric. *Nanoscale* **2021**, *13*, 13631–13640.

[31] Gaddam, V.; Kim, G.; Kim, T.; Jung, M.; Kim, C.; Jeon, S. Novel approach to high κ (~ 59) and low EOT (~ 3.8 Å) near the morphotrophic phase boundary with AFE/FE (ZrO_2/HZO) bilayer heterostructures and high-pressure annealing. *ACS Appl. Mater. Inter.* **2022**, *14*, 43463–43473.

[32] Zhang, Y. C.; Yu, J.; Zhu, R. X.; Wang, M. D.; Tan, C. W.; Tu, T.; Zhou, X. H.; Zhang, C. C.; Yu, M. S.; Gao, X. Y. et al. A single-crystalline native dielectric for two-dimensional semiconductors with an equivalent oxide thickness below 0.5 nm. *Nat. Electron.* **2022**, *5*, 643–649.

[33] Park, G.; Nguyen, A. H.; Nguyen, M. C.; Nguyen, A. D.; Kim, H.; Kim, J.; Hwang, K.; Shin, H.; Song, S.; Choi, R. Tailoring of ferroelectric coercive field and polarization with ferroelectric and antiferroelectric $Hf_xZr_{1-x}O_2$ bilayer structure. *IEEE Electron Dev. Lett.* **2024**, *45*, 1997–2000.

[34] Oh, S.; Jang, H.; Hwang, H. Accurate evaluation of high-k HZO/ZrO_2 films by morphotropic phase boundary. *IEEE Electron Dev. Lett.* **2024**, *45*, 28–31.

[35] Zhang, Y.; Lu, Z. H.; Wang, D.; Wang, J. N.; Cui, B. Y.; Wang, P.; Shuai, W. T.; Sun, Y. B.; Wang, X. W.; Wang, F. et al. Enhanced memory properties of MFIS devices through matching of capping electrode and ferroelectric HfO_2 film. *Surf. Interfaces* **2025**, *72*, 107037.

[36] Sang, X. H.; Grimley, E. D.; Schenk, T.; Schroeder, U.; LeBeau, J. M. On the structural origins of ferroelectricity in HfO_2 thin films. *Appl. Phys. Lett.* **2015**, *106*, 162905.

[37] Park, M. H.; Lee, Y. H.; Kim, H. J.; Schenk, T.; Lee, W.; Kim, K. D.; Fengler, F. P.; Mikolajick, T.; Schroeder, U.; Hwang, C. S. Surface and grain boundary energy as the key enabler of ferroelectricity in nanoscale hafnia-zirconia: a comparison of model and experiment. *Nanoscale* **2017**, *9*, 9973–9986.

[38] Liao, J. J.; Zeng, B. J.; Sun, Q.; Chen, Q.; Liao, M.; Qiu, C. G.; Zhang, Z. Y.; Zhou, Y. C. Grain size engineering of ferroelectric Zr-doped HfO_2 for the highly scaled devices applications. *IEEE Electron Dev. Lett.* **2019**, *40*, 1868–1871.

[39] Yuan, P.; Mao, G. Q.; Cheng, Y.; Xue, K. H.; Zheng, Y. Z.; Yang, Y.; Jiang, P. F.; Xu, Y. N.; Wang, Y.; Wang, Y. H. et al. Microscopic mechanism of imprint in hafnium oxide-based ferroelectrics. *Nano Res.* **2022**, *15*, 3667–3674.

[40] Gao, Z. M.; Lyu, S. X.; Lyu, H. B. Frequency dependence on polarization switching measurement in ferroelectric capacitors. *J. Semicond.* **2022**, *43*, 014102.

[41] Jia, S. J.; Liao, J. J.; Yang, Q.; Peng, R. C.; Wang, J. H.; Yan, F.; Wen, S. B.; Wang, Z. P.; Huang, J.; Bao, K. Y. et al. Developing HZO-based superlattices to enhance fatigue-resistance by charge injection suppression. *Adv. Funct. Mater.* **2025**, *35*, 2501470.

[42] Chernikova, A. G.; Kozodaev, M. G.; Negrov, D. V.; Korostylev, E. V.; Park, M. H.; Schroeder, U.; Hwang, C. S.; Markeev, A. M. Improved ferroelectric switching endurance of La-doped $Hf_{0.5}Zr_{0.5}O_2$ thin films. *ACS Appl. Mater. Interfaces* **2018**, *10*, 2701–2708.

[43] Chen, J. J.; Jin, C. J.; Yu, X.; Jia, X. L.; Peng, Y.; Liu, Y.; Chen, B.; Cheng, R.; Han, G. Q. Impact of oxygen vacancy on ferroelectric characteristics and its implication for wake-up and fatigue of HfO_2-based thin films. *IEEE Tran. Electron Dev.* **2022**, *69*, 5297–5301.

[44] Pešić, M.; Fengler, F. P. G.; Larcher, L.; Padovani, A.; Schenk, T.; Grimley, E. D.; Sang, X. H.; Lebeau, J. M.; Slesazeck, S.; Schroeder, U. et al. Physical mechanisms behind the field-cycling behavior of HfO_2-based ferroelectric capacitors. *Adv. Funct. Mater.* **2016**, *26*, 4601–4612.

[45] Cui, B. Y.; Wang, X. P.; Li, Y. C.; Wu, M. K.; Wu, Y. S.; Liu, J. H.; Li, X. X.; Ren, P. P.; Ye, S.; Ji, Z. G. et al. Back-end-of-line compatible HfO_2/ZrO_2 superlattice ferroelectric capacitor with high endurance and remnant polarization. *IEEE Electron Dev. Lett.* **2023**, *44*, 1011–1014.

[46] Pérez Ramírez, L.; Iung, T.; Yadav, V.; Lubin, C.; Schroeder, U.; Wunderwald, F.; Azevedo Antunes, L.; Kersch, A.; Back, T. C.; Weiland, C. et al. Correct quantification of oxygen vacancies in ferroelectric hafnia. *J. Appl. Phys.* **2025**, *138*, 134106.

[47] Wei, J. C.; Jiang, L. L.; Huang, M. L.; Wu, Y. N.; Chen, S. Y. Intrinsic defect limit to the growth of orthorhombic HfO_2 and (Hf, Zr)O_2 with strong ferroelectricity: First-principles insights. *Adv. Funct. Mater.* **2021**, *31*, 2104913.

[48] Wu, J. X.; Mo, F.; Saraya, T.; Hiramoto, T.; Kobayashi, M. A first-principles study on ferroelectric phase formation of Si-doped HfO_2 through nucleation and phase transition in thermal process. *Appl. Phys. Lett.* **2020**, *117*, 252904.

[49] Materano, M.; Lomenzo, P. D.; Kersch, A.; Park, M. H.; Mikolajick, T.; Schroeder, U. Interplay between oxygen defects and dopants: Effect on structure and performance of HfO_2-based ferroelectrics. *Inorg. Chem. Front.* **2021**, *8*, 2650–2672.

[50] Wu, M. K.; Cui, B. Y.; Wang, X. P.; Yuan, M. J.; Wu, Y. S.; Wen, Y. C.; Liu, J. H.; Zhang, T.; Ren, P. P.; Ye, S. et al. Insights into oxygen vacancy dynamics in HfO_2-ZrO_2 superlattice ferroelectric films: Implications for device reliability. *J. Appl. Phys.* **2024**, *136*, 144101.

[51] Zeng, B. J.; Yin, L. Y.; Liu, R. P.; Ju, C. F.; Zhang, Q. H.; Yang, Z. B.; Zheng, S. Z.; Peng, Q. X.; Yang, Q.; Zhou, Y. C. et al. Multiple polarization states in $Hf_{1-x}Zr_xO_2$ thin films by ferroelectric and antiferroelectric coupling. *Adv. Mater.* **2025**, *37*, 2411463.

[52] Liu, C.; Yang, Q. J.; Zeng, B. J.; Jiang, Y. Q.; Zheng, S. Z.; Liao, J. J.; Dai, S. W.; Zhong, X. L.; Zhou, Y. C.; Liao, M. Orientation independent growth of uniform ferroelectric $Hf_{0.5}Zr_{0.5}O_2$ thin films on silicon for high-density 3D memory applications. *Adv. Funct. Mater.* **2022**, *32*, 2209604.

[53] Hao, P. Q.; Zheng, S. Z.; Zeng, B. J.; Yu, T.; Yang, Z. B.; Liao, L. C.; Peng, Q. X.; Yang, Q. J.; Zhou, Y. C.; Liao, M. Highly enhanced polarization switching speed in HfO_2-based ferroelectric thin films via a composition gradient strategy. *Adv. Funct. Mater.* **2023**, *33*, 2301746.

[54] Lee, D. H.; Lee, Y.; Yang, K.; Park, J. Y.; Kim, S. H.; Reddy, P. R. S.; Materano, M.; Mulaosmanovic, H.; Mikolajick, T.; Jones, J. L. et al. Domains and domain dynamics in fluorite-structured ferroelectrics. *Appl. Phys. Rev.* **2021**, *8*, 021312.

[55] Jo, J. Y.; Yang, S. M.; Kim, T. H.; Lee, H. N.; Yoon, J. G.; Park, S.; Jo, Y.; Jung, M. H.; Noh, T. W. Nonlinear dynamics of domain-wall propagation in epitaxial ferroelectric thin films. *Phys. Rev. Lett.* **2009**, *102*, 045701.

[56] Yoo, H. K.; Kim, J. S.; Zhu, Z.; Choi, Y. S.; Yoon, A.; MacDonald,

M. R.; Lei, X.; Lee, T. Y.; Lee, D.; Chae, S. C. et al. Engineering of ferroelectric switching speed in Si doped HfO_2 for high-speed 1T-FERAM application. In *2017 IEEE International Electron Devices Meeting (IEDM)*, San Francisco, USA, 2017, pp 19.6.1–19.6.4.

[57] Jang, H.; Kashir, A.; Oh, S.; Hwang, H. Improvement of endurance and switching speed in $Hf_{1-x}Zr_xO_2$ thin films using a nanolaminate structure. *Nanotechnology* **2022**, *33*, 395205.

[58] Mu, X. P.; Wu, Y.; Zeng, B. J.; Jiang, J.; Zhou, Y. C.; Yin, L.; Liao, M.; Yang, Q. Polarization switching of HfO_2 ferroelectric in bulk and electrode/ferroelectric/electrode heterostructure. *npj Comput. Mater.* **2025**, *11*, 126.

[59] Ko, S. H.; Moon, S. E.; Yoon S. M. Synergistic impact of Al_2O_3 capping layer and deposition temperature for enhancing the ferroelectricity of undoped-HfO_2 thin films. *Curr. Appl. Phys.* **2025**, *71*, 1–8.

[60] Mo, S. T.; Feng, K. M.; Pang, J. L.; Ouyang, K.; Jiang, L. M.; Yang, Q.; Zhang, B.; Jiang, J. All-inorganic transparent $Hf_{0.85}Ce_{0.15}O_2$ ferroelectric thin films with high flexibility and stability. *Nano Res.* **2023**, *16*, 5065–5072.

[61] Zhou, C.; Feng, Y. P.; Ma, L. Y.; Huang, H. L.; Si, Y. Y.; Wang, H. L.; Huang, S. Z.; Li, J. X.; Kuo, C. Y.; Das. S. et al. Fatigue-free ferroelectricity in $Hf_{0.5}Zr_{0.5}O_2$ ultrathin films via interfacial design. *Nat. Commun.* **2025**, *16*, 7593.

[62] Li, Y. C.; Huang, T.; Li, X. X.; Zhu, X. N.; Zhang, D. W.; Lu, H. L. Domain switching characteristics in Ga-doped HfO_2 ferroelectric thin films with low coercive field. *Nano Lett.* **2024**, *24*, 6585–6591.

[63] Li, J. C.; Pan, W. J.; Zhu, Z. X.; Zhu, H. S.; Wang, Y. C.; Shen, S. C.; Yin, Y. W.; Li, X. G. Reduced coercive field and enhanced ferroelectric polarization of $Hf_{0.5}Zr_{0.5}O_2$ film through electric-field-assisted rapid annealing. *J. Materiomics* **2025**, *11*, 101061.

[64] Zhou, C.; Ma, L. Y.; Feng, Y. P.; Kuo, C. Y.; Ku, Y. C.; Liu, C. E.; Cheng, X. L.; Li, J. X.; Si, Y. Y.; Huang, H. L. et al. Enhanced polarization switching characteristics of HfO_2 ultrathin films via acceptor-donor co-doping. *Nat. Commun.* **2024**, *15*, 2893.

[65] Yang, K.; Jeong, H. W.; Lee, J.; Cho, Y. H.; Park, J. Y.; Choi, H.; Kim, Y. Y.; Lee, Y.; Kim, Y.; Park, M. H. Texture modulation of ferroelectric $Hf_{0.5}Zr_{0.5}O_2$ thin films by engineering the polymorphism and texture of tungsten electrodes. *J. Materiomics* **2025**, *11*, 101015.

[66] Liu, W. Y.; Liao, J. J.; Jiang, J.; Zhou, Y. C.; Chen, Q.; Mo, S. T.; Yang, Q.; Peng, Q. X.; Jiang, L. M. Highly stable performance of flexible $Hf_{0.6}Zr_{0.4}O_2$ ferroelectric thin films under multi-service conditions. *J. Mater. Chem. C* **2020**, *8*, 3878–3886.

[67] Jia, S. J.; Huang, J.; Wang, Z. P.; Zhao, F.; Jiang, J.; Liu, X. L.; Wang, J. H.; Yang, J. H.; Yan, F.; Liao, J. J. et al. Tailoring crystallization kinetics of HZO-based ferroelectric thin films for low-temperature process. *Acta Mater.* **2026**, *302*, 121670.